SINGULAR LIMIT PHENOMENON IN A NONLINEAR ELLIPTIC MODEL ARISING IN ELECTROCHEMISTRY

DANIEL FERNÁNDEZ*

Abstract. We study a singularly perturbed harmonic problem, with nonlinear Neumann boundary conditions of signed exponential type, arising in galvanic corrosion applications. We focus on the low-conductivity regime, which leads to a singular limit in which the solution presents a jump in the boundary. We prove convergence of the solution traces in the corresponding fractional Sobolev spaces, identify the interior limit solution, and obtain a sharp logarithmic energy expansion for smooth boundary junctions. The proofs rely mostly on trace Moser–Trudinger estimates for showing well-posedness and regularity, and on mollifier approximation techniques for the singular limit analysis. Numerical experiments test the predicted convergence rate.

1. Introduction

We study the elliptic model that arises in galvanic corrosion when the electrolyte potential is harmonic in the interior and the metal-electrolyte interface is governed by highly nonlinear Butler–Volmer current laws [3, 20, 24]. Related elliptic corrosion models with nonlinear boundary reactions appear, for instance, in [28, 13, 4].

The unknown ϕ_κ denotes the steady electric potential in a bounded electrolyte domain $\Omega \subset \mathbb{R}^2$. The boundary is decomposed into two reaction boundary parts Γ_a, Γ_c, and a nonempty zero-flux part Γ_N, and ϕ_κ solves

$$\begin{cases} -\Delta \phi_\kappa = 0 & \text{in } \Omega, \\ \partial_\nu \phi_\kappa = 0 & \text{on } \Gamma_N, \\ \partial_\nu \phi_\kappa = -i_a(\phi_\kappa)/\kappa & \text{on } \Gamma_a, \\ \partial_\nu \phi_\kappa = -i_c(\phi_\kappa)/\kappa & \text{on } \Gamma_c, \end{cases} \tag{1.1}$$

where ν is the exterior unit normal and $\kappa > 0$ is the electrolyte conductivity. The functions i_a and i_c are signed exponentials with distinct zeros ϕ_a and ϕ_c. In corrosion terminology, Γ_a and Γ_c are anodic and cathodic portions of the exposed interface, while Γ_N represents an insulated or nonreacting boundary part.

*Chair for Dynamics, Control, Machine Learning, and Numerics (Alexander von Humboldt Professorship), Department of Mathematics, Friedrich-Alexander-Universität Erlangen-Nürnberg, 91058 Erlangen, Germany.

Email: daniel.fernandez@fau.de.

2020 *Mathematics Subject Classification.* Primary 35B25, 35J65; Secondary 35B40, 35B65, 35J25.

Key words and phrases. Nonlinear elliptic equations, nonlinear boundary conditions, asymptotic analysis, mixed boundary value problems.

This model is meant to isolate the activation-controlled part of a galvanic cell in a regime where the electrolyte conductivity is small relative to the interfacial exchange-current scale. Equivalently, after nondimensionalization, small κ may represent a poorly conducting electrolyte, a long current path, or comparatively fast boundary charge-transfer kinetics. The analysis does not include concentration depletion, space-charge layers, evolving corrosion fronts, or changes in which boundary portions are anodic and cathodic. Those effects are important in full corrosion simulations [17, 26, 9, 31, 18], but here they are deliberately frozen in order to identify the singular elliptic mechanism created by incompatible cathodic and anodic equilibrium potentials.

The main difficulty is the *boundary singularity* generated by the cathode-anode boundary decomposition. In two dimensions the exponential Neumann law lies in the *trace-critical regime* governed by trace Moser–Trudinger estimates [6, 15, 29, 30].

As $\kappa \to 0^+$, the prefactor $1/\kappa$ forces the trace on $\Gamma_a \cup \Gamma_c$ toward the two equilibrium values. If these limiting values meet at finitely many points of $\overline{\Gamma_a} \cap \overline{\Gamma_c}$, the limiting boundary datum is discontinuous, and the critical $H^{1/2}$ cost of approximating this jump produces *logarithmic energy growth* [19, 8].

The central result of the paper is the *exact leading coefficient* of this growth. The proof isolates the three ingredients behind this phenomenon: a stiff boundary primitive that selects the equilibrium trace, a linear elliptic extension operator that propagates the trace into the interior, and the local borderline capacity of a boundary step.

1.1. **Contributions.** The main results identify the singular limit generated by the reactive boundary structure.

- **Boundary convergence and mixed harmonic selection.** Under the standing geometric assumptions (2.1)–(2.3), the solution traces $\operatorname{Tr}\phi_\kappa$ from equation (1.1) converge on the reaction boundary $\Gamma_c \cup \Gamma_a$ to the *equilibrium profile*

$$\Phi_0 := \phi_c \mathbf{1}_{\Gamma_c} + \phi_a \mathbf{1}_{\Gamma_a} \quad \text{on } \Gamma_c \cup \Gamma_a, \tag{1.2}$$

  and satisfy, for every $0 \le s < 1/2$, and sufficiently small $\kappa > 0$,

$$\| \operatorname{Tr}\phi_\kappa - \Phi_0 \|_{H^s(\Gamma_c \cup \Gamma_a)} \le C_s \, \kappa^{1/2-s} |\log \kappa|^{1/2}.$$

  The solutions converge locally in the interior to the bounded mixed harmonic function selected by Φ_0, with the quantitative interior rate inherited from the boundary estimate (Theorem 2.1 and Corollary 2.1).
- **Exact smooth boundary-jump constant.** Let J_κ be the energy functional associated with problem (1.1), and assume $\overline{\Gamma_a} \cap \overline{\Gamma_c}$ is a set of N junction points. Then,

$$J_\kappa(\phi_\kappa) = \frac{N(\phi_c - \phi_a)^2}{2\pi} |\log \kappa| + O(\log |\log \kappa|).$$

Thus the low-conductivity limit is singular: the energy cannot remain bounded when adjacent boundary pieces try to impose two different equilibrium potentials. The solutions still select the cathodic and anodic equilibrium values away from the junctions, but the transition between them is compressed into boundary layers whose total leading cost is exactly the logarithmic term above (Theorem 2.2).

- **Numerical validation and mesh design.** The finite-element experiments focus on theorem-facing diagnostics: boundary and interior convergence, normalized energy, exact-constant refinement, mesh refinement guided by the boundary-layer scale near each jump, and corrugated tests with several jump points, using standard conforming finite-element discretizations. The same local balance identifies the heuristic *reaction-layer mesh scale* $h_{\min} \simeq \kappa$ near each smooth jump point (Remark 4.1).

1.2. **Related work.** We briefly situate the paper relative to corrosion models, exponential Neumann singular limits, and the functional-analytic tools used below.

Corrosion and nonlinear boundary models. The signed exponential boundary law is the Butler–Volmer current-overpotential relation [3, 20]. Related nonlinear elliptic corrosion models address well-posedness, singular exact solutions, boundary blow-up, and heterogeneous or periodic reactions [28, 13, 4]. Those works provide the electrochemical and elliptic background, but not the low-conductivity mechanism in which a stiff boundary energy selects incompatible adjacent equilibrium traces.

Boundary concentration limits. Singular limits for exponential Neumann data often produce boundary concentration: large-amplitude solutions and rescaled fluxes converging to Dirac masses [7, 12], or, in Steklov-type variants, concentration along boundary geodesics [22]. Here the range bound prevents blow-up, and the singular object is instead a discontinuous equilibrium trace. The leading cost is therefore a fractional boundary-jump cost, not a concentration energy.

Existence and regularity of the solution. The fixed-conductivity problem relies on trace Moser–Trudinger control for exponential boundary growth [6, 30]. The singular limiting arguments also use mixed harmonic extension theory [14, 27] and standard Neumann shift results [11]. These tools supply compactness, coercivity, and interior smoothing, but not the sharp low-conductivity energy constant.

Boundary-jump cost. The local cost of smoothing a one-dimensional step is classical in fractional Sobolev theory and potential theory [19, 8], and related logarithmic energies occur in Ginzburg–Landau settings [25]. The contribution here is to show that this jump cost is selected by the Butler–Volmer boundary functional and to compute its smooth-junction leading constant.

1.3. **Outline of the paper.** Section 2 states the model and the main singular-limit results. Section 3 collects the preliminary estimates, and Section 4 gives the proofs of the main theorems. Section 5 gives the numerical validation, and Section 6 summarizes the conclusions.

2. Main results

This section fixes the mathematical setting and states the two singular-limit results proved later. The main point is that the small conductivity parameter does not merely produce a large boundary reaction; it selects a discontinuous equilibrium trace on the reactive boundary, and the cost of resolving the resulting cathode-anode jumps determines the leading asymptotic energy.

2.1. **Model setup and geometric framework.** Throughout, $\Omega \subset \mathbb{R}^2$ is a bounded, connected domain that is either $C^{1,1}$ or a Lipschitz curvilinear polygon. In the latter case, $\partial\Omega$ is a finite union of $C^{1,1}$ arcs meeting at a finite corner set $\mathcal{C}_\Omega$, and every interior angle lies in $(0, 2\pi)$. The boundary is partitioned into cathodic, anodic, and insulated arcs:

$$\partial\Omega = \overline{\Gamma_c} \cup \overline{\Gamma_a} \cup \overline{\Gamma_N}, \tag{2.1}$$

where $\Gamma_c, \Gamma_a, \Gamma_N \subset \partial\Omega$ are pairwise disjoint relatively open finite unions of boundary arcs, with $|\Gamma_c|, |\Gamma_a|, |\Gamma_N| > 0$. The finitely many arc endpoints are ignored in trace statements. We write the reactive boundary and the cathode-anode junction set as

$$\Gamma_* := \Gamma_c \cup \Gamma_a, \qquad \Sigma_* := \overline{\Gamma_c} \cap \overline{\Gamma_a}. \tag{2.2}$$

Here Σ_* is the finite cathode-anode junction set. In the curvilinear polygonal case, cathode-anode junctions are assumed to be smooth boundary points, not corners. These junctions are also assumed to stay away from the zero-flux boundary:

$$\operatorname{dist}(\Sigma_*, \mathcal{C}_\Omega) > 0, \qquad \operatorname{dist}\big(\Sigma_*, \overline{\Gamma_N}\big) > 0. \tag{2.3}$$

with $\mathcal{C}_\Omega = \emptyset$ in the $C^{1,1}$ case and the first condition then understood as vacuous. Thus each cathode-anode junction has a reactive boundary neighborhood, while the global problem contains insulated arcs or curvilinear corners elsewhere.

In this geometric setting the steady electric potential satisfies equation (1.1), where $\kappa > 0$ is the electrolyte conductivity and the Neumann boundary data are given by the signed exponential currents

$$\begin{cases} i_c(\phi) = i_{c,0}\left(\exp(C_1(\phi - \phi_c)) - \exp(-C_2(\phi - \phi_c))\right), \\ i_a(\phi) = i_{a,0}\left(\exp(A_2(\phi - \phi_a)) - \exp(-A_1(\phi - \phi_a))\right). \end{cases} \tag{2.4}$$

Here $i_{c,0}, i_{a,0}, C_1, C_2, A_1, A_2$ are positive constants and $\phi_c > \phi_a$ are the two equilibrium potentials. The currents are strictly increasing and vanish at their own equilibria. Consequently, when the prefactor $1/\kappa$ becomes large, the cathodic boundary energetically favors the value ϕ_c and the anodic boundary favors ϕ_a. If both types of arcs meet, these two preferred values are incompatible at the junction. The boundary decomposition and the resulting cathode-anode junction geometry are illustrated in Figure 1, where the planar setting used in the analysis appears as a cross-section of the three-dimensional corrosion configuration.

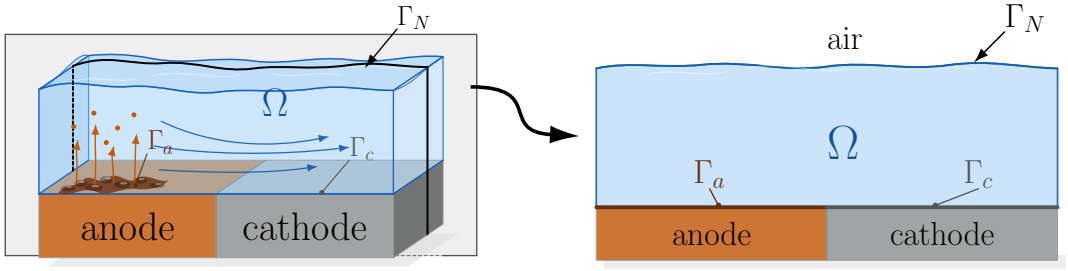

FIGURE 1. Three-dimensional corrosion sketch with an indicated slicing plane and the corresponding two-dimensional cross-section used in the model. The reduced planar domain keeps the reactive anodic and cathodic boundary pieces Γ_a, Γ_c and the insulated boundary part Γ_N that enter the mixed boundary-value problem.

2.2. **Singular-limit results.** In this subsection, we state the singular limit results in the geometric setting fixed by (2.1)–(2.3) together with the boundary-value problem (1.1). The first theorem is a convergence result: it identifies the limiting boundary trace and the harmonic interior solution selected by that trace.

The second theorem is a sharp energy result: it shows that, at smooth cathode-anode junctions, the leading energy is the half-plane boundary contribution of one jump, multiplied by the number of junctions. These conclusions separate the global compactness mechanism from the local boundary-layer calculation.

For each $\kappa > 0$, the weak formulation of (1.1) is to find $\phi_\kappa \in H^1(\Omega)$ such that

$$\int_\Omega \nabla\phi_\kappa \cdot \nabla v \, dx + \frac{1}{\kappa}\int_{\Gamma_c} i_c(\phi_\kappa)\, v \, ds + \frac{1}{\kappa}\int_{\Gamma_a} i_a(\phi_\kappa)\, v \, ds = 0 \tag{2.5}$$

for every $v \in H^1(\Omega)$. The basic solvability and regularity properties are recorded in Lemma 3.1; in particular, ϕ_κ is well defined and unique for every fixed $\kappa > 0$.

We use $H^{1/2}(\Gamma_*)$ as the restriction space of $H^{1/2}(\partial\Omega)$, equipped with the quotient trace norm

$$\|g\|_{H^{1/2}(\Gamma_*)} := \inf\{\|G\|_{H^{1/2}(\partial\Omega)} : \ G|_{\Gamma_*} = g\}.$$

For $0 \le s < 1/2$, $H^s(\Gamma_*)$ denotes the usual fractional Sobolev space on the finite union of boundary arcs, defined in arclength coordinates; endpoint values are immaterial in this range. The step trace Φ_0 defined in (1.2) belongs to $H^s(\Gamma_*)$ for every $0 \le s < 1/2$.

For $g \in H^{1/2}(\Gamma_*)$, H_*g denotes the unique function $u \in H^1(\Omega)$ with $\operatorname{Tr} u = g$ on Γ_* such that

$$\int_\Omega \nabla u \cdot \nabla v \, dx = 0 \qquad \text{for all } v \in H^1(\Omega) \text{ with } \operatorname{Tr} v = 0 \text{ on } \Gamma_*.$$

Thus H_*g is the mixed harmonic extension with homogeneous Neumann data on Γ_N.

We now state the two main results of the paper.

Theorem 2.1 (Boundary convergence in subcritical trace norms)**.** *Assume the geometric setting* (2.1)–(2.3)*. Let* $Tr\phi_\kappa$ *be the solution trace of problem* (1.1)*, and let* Φ_0 *be the step function* (1.2)*. For every* $0 \le s < 1/2$*, there is* $C_s > 0$ *such that, for*

all sufficiently small $\kappa > 0$,

$$\| \operatorname{Tr} \phi_\kappa - \Phi_0 \|_{H^s(\Gamma_*)} \le C_s \, \kappa^{1/2-s} |\log \kappa|^{1/2}, \tag{2.6}$$

Thus $\operatorname{Tr} \phi_\kappa \to \Phi_0$ *in* $H^s(\Gamma_*)$ *for every* $0 \le s < 1/2$. *The constants depend only on the domain, the boundary decomposition, the equilibrium values* ϕ_a, ϕ_c, *the fixed boundary-reaction parameters, and on* s.

The $s = 0$ boundary estimate propagates to compact subsets through interior estimates for the corresponding mixed harmonic extension.

Corollary 2.1 (Interior convergence)**.** *Under the hypotheses of Theorem 2.1, let* u_0 *be the bounded mixed harmonic extension of the boundary values* Φ_0 *on* Γ_*, *with homogeneous Neumann data on* Γ_N. *Then, for every compact set* $K \subset\subset \Omega$ *and every integer* $m \ge 0$, *there is* $C_{K,m} > 0$ *such that, for all sufficiently small* $\kappa > 0$,

$$\|\phi_\kappa - u_0\|_{C^m(K)} \le C_{K,m} (\kappa |\log \kappa|)^{1/2}.$$

Consequently, $\phi_\kappa \to u_0$ *in* $C^m_{\mathrm{loc}}(\Omega)$ *for every integer* $m \ge 0$.

The energy associated with the same weak problem (1.1) is

$$J_\kappa(\phi) := \frac{1}{2} \int_\Omega |\nabla \phi|^2 + \frac{1}{\kappa} \left(\int_{\Gamma_c} I_c(\phi(s)) \, ds + \int_{\Gamma_a} I_a(\phi(s)) \, ds \right), \tag{2.7}$$

where $I_c(\phi) := \int_{\phi_c}^{\phi} i_c(r) \, dr$ and $I_a(\phi) := \int_{\phi_a}^{\phi} i_a(r) \, dr$. These primitives are normalized to vanish at their respective equilibria; they are nonnegative and strictly convex. Lemma 3.1 also identifies ϕ_κ as the unique minimizer of J_κ.

Where Theorem 2.1 and Corollary 2.1 control the trace error and the selected interior profile, the next theorem pins down the sharp logarithmic energy constant.

Theorem 2.2 (Sharp logarithmic expansion)**.** *Assume the geometric setting (2.1)–(2.3). Let* J_κ *be the energy functional in (2.7), and assume there are* $N = \#\Sigma_*$ *junction points. Then there is* $C > 0$ *such that, for all sufficiently small* $\kappa > 0$,

$$\left| J_\kappa(\phi_\kappa) - \frac{N(\phi_c - \phi_a)^2}{2\pi} |\log \kappa| \right| \le C \log |\log \kappa|. \tag{2.8}$$

Consequently

$$\lim_{\kappa \to 0^+} \frac{J_\kappa(\phi_\kappa)}{|\log \kappa|} = \frac{N(\phi_c - \phi_a)^2}{2\pi}.$$

The remainder constant depends only on the fixed domain geometry, the boundary decomposition, the equilibrium gap $\phi_c - \phi_a$, *and the fixed boundary-reaction parameters.*

The preliminary lemmas are collected in Section 3, and the proofs of the singular-limit theorems are given in Section 4.

3. Preliminary lemmas

This section collects the analytic inputs used in the proofs: coercivity of the boundary primitives, range and regularity properties of solutions, mixed harmonic extension estimates, and the energy bounds.

Lemma 3.1 (Basic solvability and regularity)**.** *For every $\kappa > 0$, equation (1.1) admits a unique weak solution $\phi \in H^1(\Omega)$. If Ω is $C^{1,1}$, then this solution belongs to $H^{3/2}(\Omega)$ and satisfies*

$$\|\phi\|_{H^{3/2}(\Omega)} \le B e^{A\|\phi\|^2_{H^1(\Omega)}} + C'\|\phi\|_{L^2(\Omega)} \tag{3.1}$$

for suitable constants $A, B, C' > 0$, with B allowed to depend on κ. If Ω is a Lipschitz curvilinear polygon, then for every $\eta \in (0, 1/2)$ the same estimate holds with $H^{3/2-\eta}(\Omega)$ in place of $H^{3/2}(\Omega)$ and with constants allowed to depend on η.

The proof uses the following elementary coercivity estimate for the boundary primitives.

Lemma 3.2 (Quadratic lower bounds for the primitives)**.** *The boundary primitives satisfy*

$$I_c(t) \ge \frac{m_c}{2}(t-\phi_c)^2, \qquad I_a(t) \ge \frac{m_a}{2}(t-\phi_a)^2 \qquad \text{for all } t \in \mathbb{R},$$

where

$$m_c := i_{c,0}\min\{C_1, C_2\}, \qquad m_a := i_{a,0}\min\{A_1, A_2\}.$$

Proof of Lemma 3.2. Since

$$I_c''(t) = i_{c,0}\big(C_1 e^{C_1(t-\phi_c)} + C_2 e^{-C_2(t-\phi_c)}\big) \ge m_c,$$

and similarly $I_a'' \ge m_a$, Taylor's theorem at the minimizing points gives the result: $I_c(\phi_c) = I_c'(\phi_c) = 0$ and $I_a(\phi_a) = I_a'(\phi_a) = 0$. □

Proof of Lemma 3.1. We first record the exponential trace estimate needed below. The trace Moser–Trudinger inequality on the compact one-dimensional Lipschitz manifold $\partial\Omega$ implies that, for every $\lambda > 0$, there is $C_\lambda > 0$ such that

$$\int_{\partial\Omega} e^{\lambda|u|}\, ds \le C_\lambda \exp\big(C_\lambda \|u\|^2_{H^{1/2}(\partial\Omega)}\big) \qquad (u \in H^{1/2}(\partial\Omega)).$$

Indeed, this follows from the normalized trace Moser–Trudinger inequality applied to $u - \bar{u}$, Young's inequality, and the bound $|\bar{u}| \le C\|u\|_{H^{1/2}(\partial\Omega)}$; see [6, 30]. Since the signed exponential nonlinearities and their primitives have at most linear exponential growth, the trace theorem gives, for every $1 \le p < \infty$ and every $\phi \in H^1(\Omega)$,

$$\begin{aligned}&\|I_c(\phi)\|^p_{L^p(\Gamma_c)} + \|I_a(\phi)\|^p_{L^p(\Gamma_a)}\\ &\quad + \|i_c(\phi)\|^p_{L^p(\Gamma_c)} + \|i_a(\phi)\|^p_{L^p(\Gamma_a)} \le C_p \exp\big(C_p\|\phi\|^2_{H^1(\Omega)}\big).\end{aligned}$$

In particular, the boundary part of J_κ is finite on $H^1(\Omega)$ and the boundary nonlinearities belong to L^p for every finite p.

We now prove existence and uniqueness. Lemma 3.2 gives constants $m_c, m_a > 0$ such that

$$J_\kappa(\phi) \geq \frac{1}{2}\|\nabla\phi\|^2_{L^2(\Omega)} + \frac{c}{\kappa}\|\operatorname{Tr}\phi - \Phi_0\|^2_{L^2(\Gamma_a\cup\Gamma_c)}, \qquad c := \frac{1}{2}\min\{m_a, m_c\} > 0.$$

Since $\Gamma_a \cup \Gamma_c$ has positive boundary measure, the Poincaré trace inequality

$$\|\phi\|^2_{L^2(\Omega)} \leq C\big(\|\nabla\phi\|^2_{L^2(\Omega)} + \|\operatorname{Tr}\phi\|^2_{L^2(\Gamma_a\cup\Gamma_c)}\big)$$

and the boundedness of Φ_0 imply coercivity of J_κ on $H^1(\Omega)$.

Let (ϕ_n) be a minimizing sequence. Coercivity gives $\phi_n \rightharpoonup \phi$ in $H^1(\Omega)$ after passing to a subsequence, and the compact trace embedding gives $\operatorname{Tr}\phi_n \to \operatorname{Tr}\phi$ strongly in $L^2(\partial\Omega)$ and a.e. on the boundary. The boundedness of (ϕ_n) in H^1 and the exponential trace estimate above, applied with some $q > 1$, imply an L^q bound on $I_c(\phi_n)$ and $I_a(\phi_n)$ on the corresponding boundary arcs. These boundary primitives are therefore uniformly integrable. Thus, since the traces converge a.e.,

$$\int_{\Gamma_c} I_c(\phi_n)\,ds + \int_{\Gamma_a} I_a(\phi_n)\,ds \to \int_{\Gamma_c} I_c(\phi)\,ds + \int_{\Gamma_a} I_a(\phi)\,ds,$$

while the Dirichlet term is weakly lower semicontinuous. Hence J_κ attains its minimum.

The functional is strictly convex. Indeed, equality in the convexity inequality for the Dirichlet term forces two competitors to differ by a constant, and equality in the boundary terms is then impossible unless that constant is zero, because $I_c'' > 0$ and $I_a'' > 0$ on the positive-measure sets Γ_c and Γ_a. Hence the minimizer is unique. Its first variation is well defined since the exponential trace estimate gives $i_c(\phi), i_a(\phi) \in L^2$ on the boundary and the trace of every $v \in H^1(\Omega)$ lies in $L^2(\partial\Omega)$. The minimizer therefore satisfies (2.5), which is the weak form of (1.1).

It remains to prove the stated regularity. Let ϕ be the unique weak solution. The boundary datum

$$F_\phi = \begin{cases} 0 & \text{on } \Gamma_N, \\ -\dfrac{i_c(\phi)}{\kappa} & \text{on } \Gamma_c, \\ -\dfrac{i_a(\phi)}{\kappa} & \text{on } \Gamma_a \end{cases}$$

belongs to $L^2(\partial\Omega)$ by the exponential trace estimate above. More explicitly,

$$\|F_\phi\|_{L^2(\partial\Omega)} \leq \frac{\|i_c(\phi)\|_{L^2(\Gamma_c)} + \|i_a(\phi)\|_{L^2(\Gamma_a)}}{\kappa} \leq Be^{A\|\phi\|^2_{H^1(\Omega)}},$$

with B allowed to depend on the fixed value of κ. Taking $v = 1$ in (2.5) gives the compatibility condition $\int_{\partial\Omega} F_\phi\,ds = 0$. Standard Neumann regularity for $C^{1,1}$ domains [16, 11] gives

$$\|\phi\|_{H^{3/2}(\Omega)} \leq C'\big(\|F_\phi\|_{L^2(\partial\Omega)} + \|\phi\|_{L^2(\Omega)}\big),$$

which proves the estimate in the smooth-boundary case. For Lipschitz curvilinear polygons we use the corresponding Neumann shift theorem below the corner threshold: for every $\eta > 0$,

$$\|\phi\|_{H^{3/2-\eta}(\Omega)} \le C'_\eta\big(\|F_\phi\|_{L^2(\partial\Omega)} + \|\phi\|_{L^2(\Omega)}\big),$$

again from [11]. Since every Lipschitz polygonal angle lies in $(0, 2\pi)$, the first Neumann corner exponents remain larger than $1/2$, which is enough for the order used here. This proves the curvilinear polygonal statement. □

The remaining properties of the PDE solution are grouped in the following lemma.

Lemma 3.3 (Bounds on the solution and optimal regularity)**.** *Assume that Ω and the boundary decomposition satisfy (2.1)–(2.3), and let ϕ be the weak solution of (1.1), equivalently (2.5).*

(1) *If, in addition, Ω is connected, then*

$$\phi_a \le \phi(x) \le \phi_c \qquad \text{for a.e. } x \in \Omega.$$

(2) *In the $C^{1,1}$ case, the solution satisfies $\phi \in H^s(\Omega)$ for all $0 \le s < 2$. In the Lipschitz curvilinear polygonal case, $\phi \in H^{3/2-\eta}(\Omega)$ for every $\eta \in (0, 1/2)$, and $\phi \in H^s(U \cap \Omega)$ for all $0 \le s < 2$ whenever $\overline{U}$ is disjoint from the corner set $\mathcal{C}_\Omega$. Moreover, if the induced Neumann datum has a jump at a smooth boundary point, then $\phi \notin H^2(\Omega)$.*

We address the two solution-dependent items in order. The proof uses only the monotonicity structure of the signed exponential nonlinearities and the standard boundary regularity machinery already invoked in Lemma 3.1.

Proof of Lemma 3.3. **Step 1** (Range bound). For the range bound, test (2.5) with $v = (\phi - \phi_c)^+$. On $\{v > 0\}$, both $i_c(\phi)$ and $i_a(\phi)$ are nonnegative because $\phi > \phi_c > \phi_a$. Hence all terms in the weak identity are nonnegative, so

$$0 = \int_{\{v>0\}} |\nabla\phi|^2\,dx + \frac{1}{\kappa}\int_{\Gamma_c} i_c(\phi)v\,ds + \frac{1}{\kappa}\int_{\Gamma_a} i_a(\phi)v\,ds$$

forces each term to vanish. Thus v is constant on the connected domain Ω. If this constant were positive, then the trace of ϕ would be strictly larger than both limiting values on the positive-measure set $\Gamma_c \cup \Gamma_a$, making the boundary integrals strictly positive. Hence $v = 0$ and $\phi \le \phi_c$. Testing with $v = -(\phi_a - \phi)^+$ gives the lower bound in the same way: on $\{\phi < \phi_a\}$ the functions $i_a(\phi)$, $i_c(\phi)$, and v are all nonpositive, so the products $i_c(\phi)v$ and $i_a(\phi)v$ are nonnegative.

Step 2 (Regularity below H^2). The case $s = 0$ is immediate from $\phi \in H^1(\Omega)$. For the positive orders below 2, choose $\eta \in (0, 1/2)$. Lemma 3.1 gives a trace in $H^{1-\eta}$ on each relatively open boundary arc; in the $C^{1,1}$ case one may take $\eta = 0$ at this first step.

On such an arc the range bound keeps ϕ in the compact interval $[\phi_a, \phi_c]$, and the derivatives of the signed exponential nonlinearities are bounded on this interval. The Sobolev chain rule therefore gives $i_a(\phi), i_c(\phi) \in H^{1-\eta}$ along their respective arcs.

Thus the induced Neumann datum F_ϕ is piecewise $H^{1-\eta}$, with only finitely many possible jumps at arc endpoints. A one-dimensional piecewise $H^{1-\eta}$ function with finitely many jumps belongs to $H^s(\partial\Omega)$ for every $s < 1/2$: this follows by writing it as a finite sum of $H^{1-\eta}$ pieces cut off by interval indicator functions, and using $\mathbf{1}_I \in H^s$ exactly for $s < 1/2$.

The standard Neumann shift theorem on $C^{1,1}$ domains yields $\phi \in H^{s+3/2}(\Omega)$ for every $s < 1/2$, hence $\phi \in H^r(\Omega)$ for all $r < 2$ in the smooth-boundary case. In the Lipschitz curvilinear polygonal case, Lemma 3.1 gives the stated global $H^{3/2-\eta}$ regularity. Away from the finite corner set, the boundary is $C^{1,1}$ and the same local shift theorem gives $\phi \in H^r(U \cap \Omega)$ for all $r < 2$ whenever $\overline{U} \cap \mathcal{C}_\Omega = \emptyset$. Reentrant corners may limit the global Sobolev order below 2, so the polygonal conclusion is local near smooth boundary points.

Step 3 (Failure of H^2). It remains to identify when a jump is actually present. Taking $\eta < 1/2$ above, the trace has a continuous representative in a one-dimensional boundary coordinate across every smooth junction. Let $x_j \in \Sigma_*$ be a smooth Γ_c–Γ_a junction and write $\tau_j := \operatorname{Tr}\phi(x_j)$. The one-sided limits of the induced Neumann datum at x_j are

$$-i_c(\tau_j)/\kappa \qquad \text{and} \qquad -i_a(\tau_j)/\kappa,$$

in the order determined by the adjacent Γ_c and Γ_a arcs. The range bound gives $\tau_j \in [\phi_a, \phi_c]$. On this interval,

$$\begin{cases} i_c(t) \le 0, & i_c(t) = 0 \iff t = \phi_c, \\ i_a(t) \ge 0, & i_a(t) = 0 \iff t = \phi_a, \end{cases}$$

because the signed exponential nonlinearities are strictly increasing and vanish only at ϕ_c and ϕ_a, respectively. Since $\phi_a < \phi_c$, the equalities $i_c(\tau_j) = i_a(\tau_j)$ would force $\tau_j = \phi_c = \phi_a$, which is impossible. Hence the two one-sided flux limits differ, and F_ϕ has a jump at every smooth point where Γ_a and Γ_c meet.

At a smooth endpoint where one of Γ_a, Γ_c meets Γ_N, the same argument shows the exact criterion: the one-sided limits are 0 and $-i_a(\tau)/\kappa$ at a Γ_a-Neumann endpoint, or 0 and $-i_c(\tau)/\kappa$ at a Γ_c-Neumann endpoint. Thus such an endpoint is a jump of F_ϕ precisely when $\tau \neq \phi_a$ in the Γ_a case, respectively $\tau \neq \phi_c$ in the Γ_c case.

Finally, suppose one of these jumps occurs at a smooth boundary point and $\phi \in H^2(\Omega)$. In a local boundary coordinate the normal is continuous, so the trace theorem gives $\partial_\nu\phi \in H^{1/2}$ on that boundary neighborhood. This contradicts the fact that a one-dimensional jump is not in $H^{1/2}$. Hence $\phi \notin H^2(\Omega)$ whenever F_ϕ has a jump at a smooth Γ_c–Γ_a junction.

□

Lemma 3.4 (Mixed extension and Poisson smoothing)**.** *Let H_* be the mixed harmonic extension from Subsection 2.2. Then, for every $g \in H^{1/2}(\Gamma_*)$,*

$$\|\nabla H_* g\|_{L^2(\Omega)} \le C\|g\|_{H^{1/2}(\Gamma_*)}. \tag{3.2}$$

The same mixed problem has a Poisson extension $\mathcal{P}_*$, agreeing with H_* on $H^{1/2}(\Gamma_*)$ and with the harmonic-measure extension on bounded Borel data, such that

$$\|\mathcal{P}_* g\|_{C^m(K)} \le C_{K,m}\|g\|_{L^2(\Gamma_*)} \tag{3.3}$$

for every $K \subset\subset \Omega$, $m \ge 0$, and $g \in L^2(\Gamma_*)$.

Proof of Lemma 3.4. For the $H^{1/2}$ extension estimate, choose an $H^{1/2}(\partial\Omega)$ representative G of g and an $H^1(\Omega)$ lift $\widetilde{G}$. The subspace of functions in $H^1(\Omega)$ whose trace vanishes on Γ_* is closed, and the trace Poincaré inequality on the positive-measure set Γ_* gives

$$\|v\|_{H^1(\Omega)} \le C\|\nabla v\|_{L^2(\Omega)} \qquad (v \in H^1(\Omega),\ \operatorname{Tr} v = 0 \text{ on } \Gamma_*).$$

Thus the bilinear form $\int_\Omega \nabla z \cdot \nabla v$ is coercive on this closed subspace. Lax–Milgram gives a unique $z \in H^1(\Omega)$ with $\operatorname{Tr} z = 0$ on Γ_* such that

$$\int_\Omega \nabla z \cdot \nabla v\, dx = -\int_\Omega \nabla \widetilde{G} \cdot \nabla v\, dx \qquad (v \in H^1(\Omega),\ \operatorname{Tr} v = 0 \text{ on } \Gamma_*),$$

and $H_* g := \widetilde{G} + z$ is independent of the chosen lift. The same coercivity estimate gives

$$\|\nabla H_* g\|_{L^2(\Omega)} \le C\|\widetilde{G}\|_{H^1(\Omega)} \le C\|G\|_{H^{1/2}(\partial\Omega)}.$$

Taking the infimum over all representatives G proves (3.2).

The mixed problem under the finite decomposition used here admits harmonic-measure, equivalently Poisson-kernel, representations for boundary data on the Dirichlet part; see [14, 5, 21, 27]. The kernel is associated with homogeneous Neumann data on Γ_N and Dirichlet data on Γ_*. For fixed $K \subset\subset \Omega$, interior estimates applied to the kernel in the x variable imply that the kernel and all of its x-derivatives are square-integrable in the boundary variable, uniformly for $x \in K$.

Hence, the Poisson extension is well defined for $L^2(\Gamma_*)$ data and, for $|\alpha| \le m$,

$$\partial_x^\alpha \mathcal{P}_* g(x) = \int_{\Gamma_*} \partial_x^\alpha P_*(x,y) g(y)\, ds_y, \qquad \sup_{x\in K} \|\partial_x^\alpha P_*(x,\cdot)\|_{L^2(\Gamma_*)} \le C_{K,m},$$

which proves (3.3) by Cauchy's inequality. When $g \in H^{1/2}(\Gamma_*)$, uniqueness of the finite-energy mixed solution and the same boundary trace show that this Poisson extension agrees with the variational extension constructed above. For bounded Borel data the harmonic-measure formula is unchanged by altering values at finitely many endpoints. □

Lemma 3.5 (Local annular lower bound near a smooth boundary jump)**.** *Let $\Psi : B_R^+ \to \Omega \cap U$ be a $C^{1,1}$ boundary-flattening chart with $\Psi(0) \in \partial\Omega$ and $D\Psi(0)$ orthogonal, whose positive and negative flat boundary rays map, after a rigid motion, to two adjacent components of Γ_*. Fix $q_\pm \in \mathbb{R}$ and $M > 0$. Then, every $u \in H^1(\Omega)$ with $|u| \le M$ a.e. in $\Psi(B_R^+)$ satisfies, for $0 < r < R/2$,*

$$\frac{1}{2}\int_{\Psi(A_{r,R}^+)} |\nabla u|^2\, dx \ge \frac{|q_+ - q_-|^2}{2\pi} \log\frac{R}{r} - C\left(1 + Er^{-1/2}\right), \tag{3.4}$$

where $A^+_{r,R} := \{(\rho,\theta) : r < \rho < R,\ 0 < \theta < \pi\}$ *and, for* $w = u \circ \Psi$,

$$b(\rho) := \operatorname{Tr} w(\rho, 0), \qquad a(\rho) := \operatorname{Tr} w(-\rho, 0) \quad \textit{for a.e. } 0 < \rho < R,$$

$$E^2 := \int_0^R \left(|a(\rho) - q_-|^2 + |b(\rho) - q_+|^2 \right) d\rho.$$

Proof of Lemma 3.5. The trace and slicing statements used below are standard consequences of applying the Sobolev trace theorem on Lipschitz sectors and then using Fubini in polar coordinates. In particular, for a.e. $\rho \in (0, R)$ the angular slice $\theta \mapsto w(\rho, \theta)$ belongs to $H^1(0, \pi)$, its endpoint values agree with the flat boundary traces of w, and

$$\int_r^R \int_0^\pi \rho^{-1} |\partial_\theta w(\rho, \theta)|^2 \, d\theta \, d\rho < \infty.$$

For $y = (s, t) = \rho(\cos\theta, \sin\theta)$, the change of variables gives

$$\int_{\Psi(A^+_{r,R})} |\nabla u|^2 \, dx = \int_{A^+_{r,R}} A(y) \nabla w(y) \cdot \nabla w(y) \, dy,$$

where

$$A(y) = |\det D\Psi(y)| \, D\Psi(y)^{-1} D\Psi(y)^{-T}.$$

After composing Ψ with a rigid motion, $A(0) = I$. The $C^{1,1}$ bounds give $A(y)\xi \cdot \xi \geq (1 - C\rho)|\xi|^2$. Reducing R if necessary and keeping only the angular derivative,

$$\int_{\Psi(A^+_{r,R})} |\nabla u|^2 \, dx \geq \int_r^R \frac{1 - C\rho}{\rho} \int_0^\pi |\partial_\theta w(\rho, \theta)|^2 \, d\theta \, d\rho.$$

The one-dimensional endpoint inequality on each angular slice gives

$$\int_0^\pi |\partial_\theta w(\rho, \theta)|^2 \, d\theta \geq \frac{|b(\rho) - a(\rho)|^2}{\pi}.$$

Therefore

$$\int_{\Psi(A^+_{r,R})} |\nabla u|^2 \, dx \geq \int_r^R \frac{|b(\rho) - a(\rho)|^2}{\pi\rho} \, d\rho - C \int_r^R |b(\rho) - a(\rho)|^2 \, d\rho.$$

The last integral is bounded by a constant depending only on M and R. Let $d := |q_+ - q_-|$. Since

$$b - a = (q_+ - q_-) + (b - q_+) - (a - q_-),$$

we have

$$|b - a|^2 \geq d^2 - 2d \left(|b - q_+| + |a - q_-| \right).$$

By Cauchy's inequality,

$$\int_r^R \frac{|b - q_+| + |a - q_-|}{\rho} \, d\rho \leq CE \left(\int_r^R \rho^{-2} \, d\rho \right)^{1/2} \leq CEr^{-1/2}.$$

Combining these estimates and dividing by two proves (3.4). □

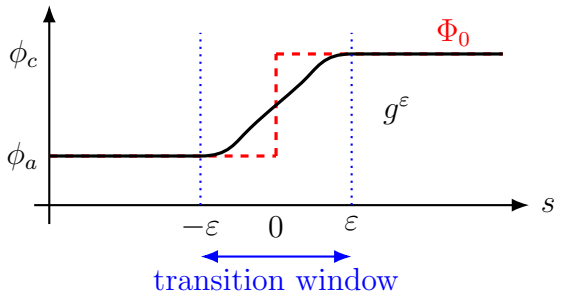

FIGURE 2. Local smoothing of the limiting boundary step near one point of Σ_*. The trace is changed only on the window $|s| \le \varepsilon$, while it remains equal to the limiting values ϕ_a and ϕ_c outside this window.

4. Proofs

We devote this section to the proofs of the main results. We begin with the proof of the singular-limit statement in Theorem 2.1.

4.1. **Proof of Theorem 2.1.**

Proof of Theorem 2.1. We divide the proof in three steps.

Step 1 (Mollified boundary traces and boundary control). We first construct the only competitor needed for this proof. Under (2.1)–(2.3), there are $\varepsilon_0 \in (0,1)$ and $c, C > 0$ such that for each $0 < \varepsilon < \varepsilon_0$ one can choose $g^\varepsilon \in H^{1/2}(\Gamma_*)$ satisfying

$$\|g^\varepsilon - \Phi_0\|^2_{L^2(\Gamma_*)} \le C\varepsilon, \qquad \|g^\varepsilon\|^2_{H^{1/2}(\Gamma_*)} \le C|\log\varepsilon|, \tag{4.1}$$

and, for every $0 \le s < 1/2$,

$$\|g^\varepsilon - \Phi_0\|_{H^s(\Gamma_*)} \le C_s \varepsilon^{1/2-s}. \tag{4.2}$$

Moreover, $g^\varepsilon = \Phi_0$ outside an $O(\varepsilon)$ neighborhood of Σ_* and $\phi_a \le g^\varepsilon \le \phi_c$. If $\phi^\varepsilon := H_* g^\varepsilon$, then

$$\|\nabla \phi^\varepsilon\|^2_{L^2(\Omega)} \le C|\log\varepsilon|. \tag{4.3}$$

Finally, every $\phi \in H^1(\Omega)$ satisfies the boundary-control estimate

$$\kappa J_\kappa(\phi) \ge c\|\operatorname{Tr}\phi - \Phi_0\|^2_{L^2(\Gamma_*)}. \tag{4.4}$$

When junctions are present, the construction is by one-dimensional mollification of the boundary step around each point of Σ_*, with the constant values preserved away from the mollification windows; see Figure 2.

If $\Sigma_* = \emptyset$, set $g^\varepsilon = \Phi_0$. Since Φ_0 is then constant up to the endpoints of each component of Γ_*, a fixed piecewise H^1 extension across the Γ_N segments gives a representative on $\partial\Omega$ with $H^{1/2}$ norm bounded independently of ε; the L^2 and subcritical errors vanish.

Assume now that $\Sigma_* \neq \emptyset$. By the separation condition, choose pairwise disjoint arclength intervals $(-2L_j, 2L_j)$ around the jumps, contained in Γ_* and disjoint from $\overline{\Gamma_N}$, with L_j independent of ε. Then fix ε_0 so small that $2\varepsilon < L_j$ in every selected

interval whenever $0 < \varepsilon < \varepsilon_0$. In the interval centered at a jump, write the local coordinate as $s = 0$ and replace the step by

$$f^\varepsilon(s) = \phi_a + (\phi_c - \phi_a)\eta(s/\varepsilon),$$

after interchanging ϕ_a, ϕ_c if the orientation is reversed. Here $\eta \in C^\infty(\mathbb{R})$ is nondecreasing, $0 \le \eta \le 1$, $\eta = 0$ on $(-\infty, -1]$, and $\eta = 1$ on $[1, \infty)$. Away from the selected intervals we keep the exact constant values on Γ_*. Thus g^ε changes Φ_0 only in the union of transition intervals of total length $O(\varepsilon)$ and remains in $[\phi_a, \phi_c]$. Since $|g^\varepsilon - \Phi_0| \le |\phi_c - \phi_a|$ pointwise, this gives the L^2 part of (4.1).

The same local scaling gives the subcritical fractional approximation. For one transition, the difference $f^\varepsilon - \Phi_0$ has the form $F(s/\varepsilon)$ on $(-\varepsilon, \varepsilon)$ and is zero outside, where F is a fixed bounded compactly supported step-profile difference. Since $F \in H^s(\mathbb{R})$ for every $s < 1/2$,

$$\|f^\varepsilon - \Phi_0\|_{H^s(-L,L)} \le C_s \varepsilon^{1/2-s}, \qquad 0 \le s < 1/2.$$

The transition intervals are disjoint and finite in number, while cross terms between different intervals are separated by a fixed distance. Summing over the transitions proves (4.2).

It remains to record the $H^{1/2}$ cost. For one smoothed jump on a fixed interval $(-L, L)$, it is enough to estimate the Gagliardo seminorm

$$\iint_{(-L,L)^2} \frac{|f^\varepsilon(s) - f^\varepsilon(t)|^2}{|s-t|^2}\, ds\, dt \le C|\log \varepsilon|.$$

Split the integral into the regions $|s - t| \le \varepsilon$ and $|s - t| > \varepsilon$. On the first region, f^ε is C/ε-Lipschitz and is nonconstant only when at least one point lies in $(-\varepsilon, \varepsilon)$. Hence

$$\iint_{\substack{|s-t|\le\varepsilon \\ (-\varepsilon,\varepsilon)\cap\{s,t\}\neq\emptyset}} \frac{|f^\varepsilon(s) - f^\varepsilon(t)|^2}{|s-t|^2}\, ds\, dt \le C \int_{-\varepsilon}^{\varepsilon} \int_{|h|\le\varepsilon} \frac{1}{\varepsilon^2}\, dh\, ds \le C.$$

On the second region, $|f^\varepsilon(s) - f^\varepsilon(t)| \le C$ and the only logarithmic contribution comes from pairs lying on opposite sides of the transition, with separation at least ε. This gives

$$C \int_\varepsilon^{2L} \frac{dr}{r} \le C|\log \varepsilon|.$$

All other pairs either see the same constant value or are separated from the transition by a fixed distance, hence contribute $O(1)$. Pairs belonging to two different transition-point neighborhoods are also separated by a fixed distance and contribute only $O(1)$ because g^ε is uniformly bounded.

To estimate the quotient norm, we construct one admissible representative on the full boundary. For each selected transition interval choose a slightly larger arclength interval compactly contained in the same component of Γ_*, and let χ_j be a fixed smooth cutoff which is equal to one on the transition interval and vanishes outside the larger one. On Γ_* we keep the values of g^ε. On the rest of $\partial\Omega$ we define a function G^ε as follows: on each Γ_N segment, use a fixed piecewise H^1 interpolant

joining the two endpoint values inherited from the adjacent components of Γ_*. Thus $G^\varepsilon|_{\Gamma_*} = g^\varepsilon$, so by the definition of the quotient norm,

$$\|g^\varepsilon\|_{H^{1/2}(\Gamma_*)} \le \|G^\varepsilon\|_{H^{1/2}(\partial\Omega)}.$$

It remains only to bound the right-hand side. In arclength coordinates, multiplication by each fixed cutoff χ_j is bounded on $H^{1/2}$, with a constant independent of ε. Hence the pieces containing the smoothed transitions have the same $C|\log\varepsilon|$ squared $H^{1/2}$ bound obtained above. The remaining pieces of Γ_* are constant, while the interpolants on the Γ_N segments are fixed piecewise H^1 functions; all of these contribute $O(1)$ to the $H^{1/2}(\partial\Omega)$ norm. Finally, cross terms between distinct pieces are uniformly bounded because their supports are either separated by a fixed positive arclength distance or the traces match at the common endpoint through the chosen fixed interpolant. Therefore

$$\|G^\varepsilon\|^2_{H^{1/2}(\partial\Omega)} \le C|\log\varepsilon|,$$

and the quotient norm has the same bound. This proves the $H^{1/2}$ part of (4.1).

The energy estimate (4.3) follows from Lemma 3.4, specifically (3.2), and (4.1). To prove (4.4), let $m_c, m_a > 0$ be the lower curvature constants supplied by Lemma 3.2. Then

$$\int_{\Gamma_c} I_c(\phi)\,ds + \int_{\Gamma_a} I_a(\phi)\,ds \ge \frac{1}{2}\min\{m_c, m_a\}\|\operatorname{Tr}\phi - \Phi_0\|^2_{L^2(\Gamma_*)}.$$

Since $\Gamma_* = \Gamma_c \cup \Gamma_a$ up to finitely many endpoints and the Dirichlet term in J_κ is nonnegative, (4.4) follows after renaming the positive constant.

Step 2 (The L^2 trace estimate). Using the competitor $\phi^\varepsilon = H_* g^\varepsilon$ from Step 1,

$$\kappa J_\kappa(\phi^\varepsilon) \le C\kappa|\log\varepsilon| + \int_{\Gamma_c} I_c(g^\varepsilon)\,ds + \int_{\Gamma_a} I_a(g^\varepsilon)\,ds.$$

The boundary integrals vanish where $g^\varepsilon = \Phi_0$ because $I_c(\phi_c) = I_a(\phi_a) = 0$. On the remaining arcs the total length is $O(\varepsilon)$, and I_a, I_c are bounded on $[\phi_a, \phi_c]$. Thus $\kappa J_\kappa(\phi^\varepsilon) \le C(\kappa|\log\varepsilon| + \varepsilon)$. Minimality of ϕ_κ and the boundary-control estimate (4.4) yield

$$\|\operatorname{Tr}\phi_\kappa - \Phi_0\|^2_{L^2(\Gamma_*)} \le C\big(\kappa|\log\varepsilon| + \varepsilon\big).$$

Taking $\varepsilon = \kappa$ gives the $s = 0$ estimate

$$\|\operatorname{Tr}\phi_\kappa - \Phi_0\|^2_{L^2(\Gamma_*)} \le C\kappa|\log\kappa|. \tag{4.5}$$

The same comparison also gives

$$J_\kappa(\phi_\kappa) \le C|\log\kappa|.$$

The Dirichlet part of this energy bound, the trace theorem, and the range bound from Lemma 3.3(i) imply

$$\|\operatorname{Tr}\phi_\kappa\|_{L^2(\Gamma_*)} \le C, \qquad \|\operatorname{Tr}\phi_\kappa\|_{H^{1/2}(\partial\Omega)} \le C|\log\kappa|^{1/2}.$$

Step 3 (Upgrade to subcritical trace norms). Fix $0 < s < 1/2$, and let g^κ be the mollified trace from Step 1 with $\varepsilon = \kappa$. Write

$$\operatorname{Tr}\phi_\kappa - \Phi_0 = \big(\operatorname{Tr}\phi_\kappa - g^\kappa\big) + \big(g^\kappa - \Phi_0\big).$$

(4.1)–(4.2) give

$$\|g^\kappa - \Phi_0\|_{H^s(\Gamma_*)} \le C_s\kappa^{1/2-s}, \qquad \|g^\kappa\|_{H^{1/2}(\Gamma_*)} \le C|\log\kappa|^{1/2}.$$

Moreover, by (4.5) and the L^2 part of (4.1),

$$\|\operatorname{Tr}\phi_\kappa - g^\kappa\|_{L^2(\Gamma_*)} \le C(\kappa|\log\kappa|)^{1/2},$$

and the preceding trace bound gives

$$\|\operatorname{Tr}\phi_\kappa - g^\kappa\|_{H^{1/2}(\Gamma_*)} \le C|\log\kappa|^{1/2}.$$

By real interpolation on quotient spaces [16, 1] and the endpoint extension result for the subcritical range [8], this last difference satisfies

$$\|\operatorname{Tr}\phi_\kappa - g^\kappa\|_{H^s(\Gamma_*)} \le C_s\|\operatorname{Tr}\phi_\kappa - g^\kappa\|_{L^2(\Gamma_*)}^{1-2s}\|\operatorname{Tr}\phi_\kappa - g^\kappa\|_{H^{1/2}(\Gamma_*)}^{2s} \le C_s\kappa^{1/2-s}|\log\kappa|^{1/2}.$$

Combining the last two estimates gives (2.6). The case $s = 0$ is exactly (4.5). This proves convergence in $H^s(\Gamma_*)$ for every $0 \le s < 1/2$.

□

4.2. **Proof of Corollary 2.1.**

Proof of Corollary 2.1. Let $g_\kappa := \operatorname{Tr}\phi_\kappa - \Phi_0$ on Γ_*. Since $u_0 = \mathcal{P}_*\Phi_0$ and $\phi_\kappa = \mathcal{P}_*(\operatorname{Tr}\phi_\kappa)$, linearity of the Poisson extension from Lemma 3.4 gives

$$\phi_\kappa - u_0 = \mathcal{P}_* g_\kappa.$$

Indeed, both sides are harmonic in Ω, have trace g_κ on Γ_*, and satisfy the same homogeneous Neumann condition on Γ_N; uniqueness holds in the Poisson class fixed in Lemma 3.4. The smoothing estimate (3.3) from Lemma 3.4 gives

$$\|\mathcal{P}_* g_\kappa\|_{C^m(K)} \le C_{K,m}\|g_\kappa\|_{L^2(\Gamma_*)}.$$

The boundary estimate (4.5), with the dependence recorded in Theorem 2.1, gives the stated rate. The C^m_{loc} convergence follows from this estimate. For the local H^1 convergence, fix $K \subset\subset K' \subset\subset \Omega$ and set $w_\kappa := \phi_\kappa - u_0$. Since w_κ is harmonic in K', the interior Caccioppoli estimate gives; see [10],

$$\int_K |\nabla w_\kappa|^2\,dx \le \frac{C}{\operatorname{dist}(K,\partial K')^2}\int_{K'} |w_\kappa|^2\,dx.$$

The right-hand side tends to zero by the already proved local L^2 convergence on K', and therefore $\phi_\kappa \to u_0$ in $H^1(K)$. □

We next turn from trace selection to the sharp logarithmic expansion of the energy. The proof of Theorem 2.2 uses the same local boundary charts, now with matching upper and lower half-annular estimates near the Γ_c–Γ_a junctions.

4.3. **Proof of Theorem 2.2.**

Proof of Theorem 2.2. We divide the proof in four steps.

Step 1 (Reduction and charts). Let $N = \#\Sigma_*$. If $N = 0$, the absence of points where Γ_a and Γ_c meet and the separation condition allow an H^1 competitor whose trace on $\Gamma_a \cup \Gamma_c$ is exactly the limiting trace Φ_0. Its boundary primitive vanishes, so $J_\kappa(\phi_\kappa) = O(1)$, which is $O(\log|\log\kappa|)$ for small κ. We therefore assume $N > 0$ and put

$$C_N := \frac{N(\phi_c - \phi_a)^2}{2\pi}.$$

At the Γ_c–Γ_a junctions, choose one radius $R > 0$ such that the flattening neighborhoods $\Psi_j(B_R^+)$ are pairwise disjoint, avoid Γ_N, and have uniformly bounded $C^{1,1}$ norms and inverse $C^{1,1}$ norms. After a rigid motion in the reference variables, each $D\Psi_j(0)$ is the identity. Shrinking R if necessary, the pullback metric matrices below satisfy the uniform estimates used in the lower-bound step. All constants are uniform in j because only finitely many charts are used.

Step 2 (Upper-bound competitors). We claim that there are constants $\varepsilon_0, C > 0$ such that, for every $0 < \varepsilon < \varepsilon_0$, one can find $v^\varepsilon \in H^1(\Omega)$ with $\phi_a \le v^\varepsilon \le \phi_c$ a.e., whose trace differs from Φ_0 on $\Gamma_a \cup \Gamma_c$ only inside an $O(\varepsilon)$ neighborhood of Σ_*, and such that

$$\frac{1}{2}\int_\Omega |\nabla v^\varepsilon|^2\,dx \le C_N|\log\varepsilon| + C, \tag{4.6}$$

$$\int_{\Gamma_c} I_c(v^\varepsilon)\,ds + \int_{\Gamma_a} I_a(v^\varepsilon)\,ds \le C\varepsilon. \tag{4.7}$$

In a fixed transition-point neighborhood, write q_+ and q_- for the values of Φ_0 on the positive and negative boundary rays. Then $|q_+ - q_-| = \phi_c - \phi_a$. In polar coordinates (ρ,θ) on B_R^+, define

$$P(\rho,\theta) := q_+ + \frac{q_- - q_+}{\pi}\theta, \qquad 0 < \theta < \pi.$$

This profile is harmonic, takes the endpoint values q_+ and q_- on the two boundary rays, and satisfies $|\nabla P| = (\phi_c - \phi_a)/(\pi\rho)$. The corresponding flattened half-annular construction is shown in Figure 3.

Let χ_ε be a smooth radial cutoff with $\chi_\varepsilon = 0$ on $\rho \le \varepsilon$, $\chi_\varepsilon = 1$ on $\rho \ge 2\varepsilon$, and $|\chi_\varepsilon'| \le C/\varepsilon$. Put $\bar q = (q_+ + q_-)/2$ and

$$P^\varepsilon := \bar q + \chi_\varepsilon(\rho)(P - \bar q) \qquad \text{in } B_{R/2}^+.$$

Then $P^\varepsilon \in H^1(B_{R/2}^+)$, stays in $[\phi_a, \phi_c]$, and differs from the limiting trace on the flat boundary only for $|s| \le 2\varepsilon$. The energy in $B_{2\varepsilon}^+ \setminus B_\varepsilon^+$ is bounded uniformly in ε: indeed $|\nabla P| \le C/\rho$, $|\chi_\varepsilon'| \le C/\varepsilon$, and $|P - \bar q| \le C$, so the two terms in

$$\nabla P^\varepsilon = \chi_\varepsilon \nabla P + \chi_\varepsilon'(P - \bar q)e_\rho$$

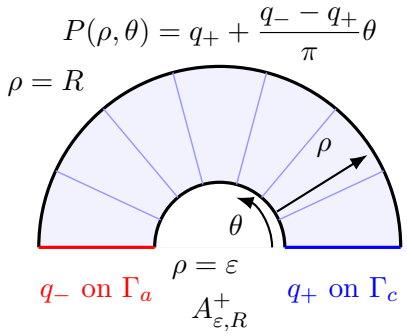

FIGURE 3. Flattened half-annular profile near a smooth boundary jump. The flat boundary carries the two limiting values q_- and q_+, and the angular harmonic interpolation on $\varepsilon < \rho < R$ gives the logarithmic Dirichlet contribution.

have square integrals bounded by constants over an annulus of radii comparable to ε. On $B^+_{R/2} \setminus B^+_{2\varepsilon}$ one has $P^\varepsilon = P$, and therefore

$$\frac{1}{2}\int_{B^+_{R/2}\setminus B^+_{2\varepsilon}} |\nabla P^\varepsilon|^2 = \frac{(\phi_c - \phi_a)^2}{2\pi}\log\frac{R}{4\varepsilon}.$$

On the fixed annulus $B^+_R \setminus B^+_{R/2}$, choose once and for all a connector $W \in H^1(B^+_R \setminus B^+_{R/2})$ whose trace equals $P(R/2,\theta)$ on the inner semicircle, equals q_- and q_+ on the negative and positive flat boundary segments, and is smooth on the outer semicircle. Such a connector follows from the trace extension theorem on the fixed Lipschitz half-annulus, and its energy is independent of ε.

Outside the union of the transition-point neighborhoods, remove the pulled-back half-disks $\Psi_j(B^+_R)$ and work on the remaining fixed Lipschitz domain. The boundary data there consist of the exact constants ϕ_a, ϕ_c on Γ_a and Γ_c, the fixed traces supplied on the outer semicircles by the connectors, and arbitrary fixed bounded traces on Γ_N. These data are mutually compatible at the endpoints of each transition-point neighborhood because the connectors preserve the flat-side values $q_\pm$. A fixed trace-extension theorem on this fixed perforated domain gives an exterior function with $O(1)$ energy, uniformly in ε.

It remains to pass from the flattened half-disk to Ω. If $y = (s,t)$ and $x = \Psi_j(y)$, then the Dirichlet integral of a pullback profile has the form

$$\int_{\Psi_j(E)} |\nabla_x v|^2\,dx = \int_E A_j(y)\nabla_y(v\circ\Psi_j)\cdot\nabla_y(v\circ\Psi_j)\,dy,$$

for each reference subdomain $E \subset B^+_R$, where $A_j(0) = I$ because $D\Psi_j(0)$ is orthogonal. The $C^{1,1}$ regularity gives $|A_j(y) - I| \le C|y|$. Therefore the metric error on the principal annulus is bounded by

$$C\int_{2\varepsilon}^{R/2} \rho\,\frac{(\phi_c - \phi_a)^2}{\rho^2}\,\rho\,d\rho \le C,$$

and the fixed inner and outer annuli remain $O(1)$. Summing over the disjoint transition-point neighborhoods proves (4.6). The boundary primitive is zero wherever the trace equals Φ_0; its support on the part of $\Gamma_a \cup \Gamma_c$ where the trace is modified has total length $O(\varepsilon)$, and I_a, I_c are bounded on $[\phi_a, \phi_c]$. This proves (4.7).

Minimality and the choice $\varepsilon = \kappa$ now give

$$J_\kappa(\phi_\kappa) \le C_N |\log \kappa| + C.$$

Step 3 (Lower bound for traces). We next prove the converse estimate needed for the minimizer. Suppose $u_\kappa \in H^1(\Omega)$ satisfies $\phi_a \le u_\kappa \le \phi_c$ a.e. and, for some fixed $B > 0$,

$$\| \operatorname{Tr} u_\kappa - \Phi_0 \|^2_{L^2(\Gamma_*)} \le B\kappa |\log \kappa|.$$

Then, for all sufficiently small κ,

$$\frac{1}{2} \int_\Omega |\nabla u_\kappa|^2 \, dx \ge C_N |\log \kappa| - C \log |\log \kappa|. \tag{4.8}$$

Set

$$e_\kappa^2 := \| \operatorname{Tr} u_\kappa - \Phi_0 \|^2_{L^2(\Gamma_*)}, \qquad r_\kappa := \kappa |\log \kappa|^2.$$

Then $e_\kappa^2 / r_\kappa \le B / |\log \kappa|$. Use the charts fixed in Step 1. Their boundary Jacobians are uniformly comparable to one, so L^2 estimates on the boundary and in flat coordinates differ only by fixed multiplicative constants.

Fix one transition point. On the positive and negative flat boundary rays let q_+ and q_- be the corresponding values of Φ_0, so $|q_+ - q_-| = \phi_c - \phi_a$. Define

$$a_{\kappa,j}(\rho) := \operatorname{Tr}(u_\kappa \circ \Psi_j)(-\rho, 0), \qquad b_{\kappa,j}(\rho) := \operatorname{Tr}(u_\kappa \circ \Psi_j)(\rho, 0).$$

The global trace estimate gives the local bound

$$E^2_{\kappa,j} := \int_0^R \left(|a_{\kappa,j}(\rho) - q_-|^2 + |b_{\kappa,j}(\rho) - q_+|^2 \right) d\rho \le C e_\kappa^2.$$

By the range assumption, $|u_\kappa|$ is uniformly bounded by a constant depending only on ϕ_a, ϕ_c. Applying Lemma 3.5 with $r = r_\kappa$ gives

$$\frac{1}{2} \int_{\Psi_j(A^+_{r_\kappa, R})} |\nabla u_\kappa|^2 \, dx \ge \frac{(\phi_c - \phi_a)^2}{2\pi} \log \frac{R}{r_\kappa} - C \left(1 + E_{\kappa,j} r_\kappa^{-1/2} \right).$$

Since $E_{\kappa,j} r_\kappa^{-1/2} \le C |\log \kappa|^{-1/2}$, the error term is bounded uniformly in κ. Therefore

$$\frac{1}{2} \int_{\Psi_j(A^+_{r_\kappa, R})} |\nabla u_\kappa|^2 \, dx \ge \frac{(\phi_c - \phi_a)^2}{2\pi} \log \frac{R}{r_\kappa} - C.$$

The annular neighborhoods are disjoint for different j, and

$$\log \frac{R}{r_\kappa} = |\log \kappa| - 2 \log |\log \kappa| + \log R.$$

Summing over the N points in Σ_* proves (4.8).

Step 4 (Conclusion for the minimizer). Theorem 2.1 gives

$$\| \operatorname{Tr} \phi_\kappa - \Phi_0 \|^2_{L^2(\Gamma_*)} \le C\kappa |\log \kappa|,$$

By the range bound from Lemma 3.3(i), Step 3 applies with $u_\kappa = \phi_\kappa$. Since the boundary part of J_κ is nonnegative,

$$J_\kappa(\phi_\kappa) \geq C_N |\log \kappa| - C \log |\log \kappa|.$$

Combining this with the upper bound from Step 2 proves (2.8).

□

Remark 4.1 (Mesh scale near smooth boundary jumps)**.** The sharp upper-bound construction in the proof of Theorem 2.2 also identifies the inner length scale in the local construction. Each jump point has a small Γ_*-neighborhood disjoint from $\overline{\Gamma_N}$, so the calculation is local. Near a smooth point where Γ_a and Γ_c meet, flatten the boundary and write the two limiting trace values as q_- and q_+. For a length scale δ, use in the half-disk the angular interpolation

$$P(\rho, \theta) = q_+ + \frac{q_- - q_+}{\pi}\theta, \qquad 0 < \theta < \pi,$$

on the annulus $\delta < \rho < R$, cut it off to the average $(q_- + q_+)/2$ on $\rho \leq \delta$, and connect it to fixed outer data on $\rho = R$. Repeating that construction with the inner cutoff radius δ and keeping the exact limiting trace away from the δ-neighborhood of Σ_* gives competitors v_κ^δ with principal Dirichlet contribution

$$\frac{1}{2}\int_\Omega |\nabla v_\kappa^\delta|^2 \, dx = \frac{N(\phi_c - \phi_a)^2}{2\pi} \log \frac{1}{\delta} + O(1), \tag{4.9}$$

with $O(1)$ uniform in δ. The boundary integral terms vanish on $\{|s| \geq \delta\} \cap \Gamma_*$ since the trace equals Φ_0 there, and on $\{|s| < \delta\}$ they are controlled by the bounded primitives I_a, I_c on $[\phi_a, \phi_c]$, giving

$$\frac{1}{\kappa}\left(\int_{\Gamma_c \cap \{|s|<\delta\}} I_c(v_\kappa^\delta)\, ds + \int_{\Gamma_a \cap \{|s|<\delta\}} I_a(v_\kappa^\delta)\, ds\right) \leq \frac{C\delta}{\kappa}. \tag{4.10}$$

At one smooth jump the same construction gives the reduced cost

$$F_{\kappa,j}(\delta) := \frac{(\phi_c - \phi_a)^2}{2\pi} \log \frac{1}{\delta} + \frac{C_j \delta}{\kappa} + O(1),$$

where $C_j > 0$ depends on the chosen inner cutoff, the functions I_a, I_c, and the chart, but not on κ or δ. This reduced cost has a stationary point satisfying

$$\delta_{\kappa,j}^* = \frac{(\phi_c - \phi_a)^2}{2\pi C_j}\, \kappa.$$

Thus this balance fixes the local order of the transition scale. Summing over the finitely many junctions gives the sharp leading logarithmic constant in Theorem 2.2; each smooth jump retains the same local length scale $\delta_{\kappa,j}^* \simeq \kappa$.

For a P^1 discretization this provides a mesh-design heuristic: κ-robust grids should use boundary elements of size $h_{\min} \approx \kappa$ near each smooth point where Γ_a and Γ_c meet and grade away from Σ_*.

5. Numerical validation

We perform finite-element experiments to test the boundary convergence, interior selection, sharp energy coefficient, and mesh rule from Subsection 2.2.

5.1. **Test problems and discrete setup.** Unless otherwise stated, the numerical values of the electrochemical parameters are those in Table 1.

Table 1. Baseline electrochemical parameters used in the numerical benchmarks.

Parameter	Value	Role
ϕ_c	0.2	cathodic equilibrium potential
ϕ_a	-0.2	anodic equilibrium potential
$i_{c,0}$	3.0×10^{-4}	cathodic exchange-current scale
$i_{a,0}$	3.0×10^{-2}	anodic exchange-current scale
$C_1 = A_2$	83.13	positive exponential slopes
$C_2 = A_1$	35.63	negative exponential slopes

Let V_h be the conforming P_1 finite-element space on the corresponding triangular mesh. The computed solution $\phi_{\kappa,h} \in V_h$ is the minimizer of

$$J_{\kappa,h}(v_h) := \frac{1}{2}\int_\Omega |\nabla v_h|^2\,dx + \frac{1}{\kappa}\left(\int_{\Gamma_c} I_c(v_h)\,ds + \int_{\Gamma_a} I_a(v_h)\,ds\right), \qquad v_h \in V_h. \tag{5.1}$$

Strict convexity gives a unique discrete minimizer. The mixed harmonic reference $u_{0,h}^{\mathrm{mix}}$ is computed on the same mesh as the nonlinear solution.

In the experiments, we report

$$C_N := \frac{N(\phi_c - \phi_a)^2}{2\pi},$$

where N is the number of smooth points where Γ_a and Γ_c meet in the benchmark, and

$$R_b(\kappa) := \frac{\|\phi_{\kappa,h} - \Phi_0\|^2_{L^2(\Gamma_*)}}{\kappa|\log\kappa|},$$
$$R_E(\kappa) := \frac{J_{\kappa,h}(\phi_{\kappa,h})}{C_N|\log\kappa|},$$
$$E_K(\kappa) := \|\phi_{\kappa,h} - u_{0,h}^{\mathrm{mix}}\|_{L^2(K)},$$

measure the boundary, energy, and interior diagnostics, with the compact set K specified in the corresponding benchmark.

The nonlinear systems are solved by damped Newton from $\kappa = 1$ downward, with sparse direct solves and an L-BFGS-B fallback only when Newton stagnates. A point is certified if

$$\|\nabla I(\lambda_h)\|_{\ell^\infty} \le 10^{-9}\max\{1, \|\nabla I(\lambda_h^{(0)})\|_{\ell^\infty}\},$$

where $\lambda_h^{(0)}$ is the initial guess. The P_1 Dirichlet term is assembled exactly on each triangle, and the nonlinear boundary terms are evaluated by a four-point Gauss–Legendre rule on each reactive boundary edge. Newton uses an Armijo backtracking

line search with tolerance 10^{-10} and step tolerance 10^{-12}; the L-BFGS-B fallback uses the same box $[\phi_a, \phi_c]$ and a maximum of 4000 iterations. The experiments were run with Python 3.13.9.

5.2. **Single boundary-jump diagnostics.** The first benchmark isolates boundary and interior convergence on the rectangle

$$L_x = 0.02, \qquad L_y = 0.01, \qquad \Omega_{\mathrm{rec}} = [0, L_x] \times [0, L_y], \qquad \Gamma_* = [0, L_x] \times \{0\},$$

with homogeneous Neumann data on the other three sides. The bottom side is split into one cathodic interval and one anodic interval,

$$\Gamma_c = [0, L_x/2] \times \{0\}, \qquad \Gamma_a = [L_x/2, L_x] \times \{0\},$$

up to the common endpoint, so $N = 1$. For the interior diagnostic in this single-jump benchmark we use

$$K = [0.25L_x, 0.75L_x] \times [0.25L_y, 0.75L_y].$$

Figure 4 shows $\phi_{\kappa,h}$ at $\kappa = 10^{-3}$, 10^{-5}, and 10^{-7}. The boundary transition sharpens near the jump point, while the interior field approaches the harmonic limit.

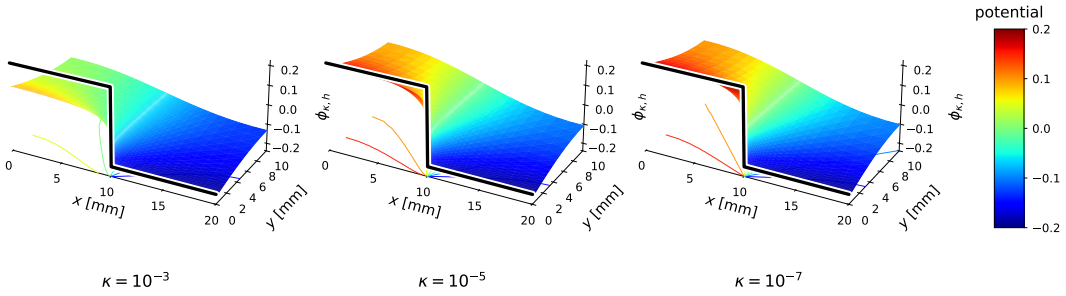

FIGURE 4. Three-dimensional single-jump evolution. From **left** to **right**, the finite-element potential sheet $\phi_{\kappa,h}(x, y)$ at $\kappa = 10^{-3}$, 10^{-5}, and 10^{-7}, with projected level curves on the base plane. The black curve along $y = 0$ marks the prescribed step boundary datum Φ_0.

Figure 5 provides the quantitative checks. The L^2 boundary-error slope is 1.065, consistent with the $s = 0$ part of Theorem 2.1, namely bounded $R_b(\kappa)$. The sampled $C^0(K)$ and $C^1(K)$ slopes are 0.798 and 0.725 in this window; these faster observed decays are consistent with the scale from Corollary 2.1.

5.3. **Multiple boundary-jump diagnostics.** These tests check whether the normalized leading coefficient is local in the number of smooth jump points and insensitive to moderate changes in the zero-flux part of the geometry. The rectangular multi-jump benchmark uses the same rectangle Ω_{rec} and bottom side Γ_* as the single-jump test, but with four alternating intervals of equal length,

$$[0, L_x/4], \quad [L_x/4, L_x/2], \quad [L_x/2, 3L_x/4], \quad [3L_x/4, L_x],$$

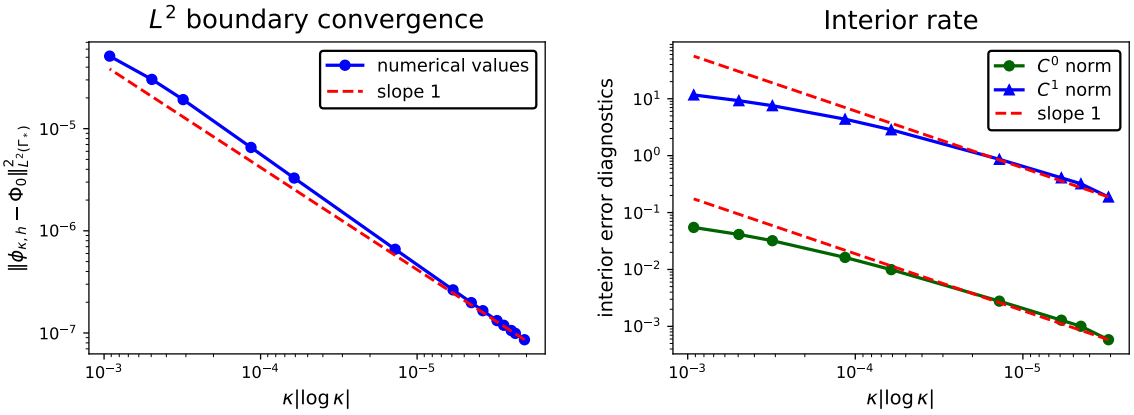

FIGURE 5. Single-rectangle theorem dashboard. **Left**: the $s = 0$ boundary convergence diagnostic from Theorem 2.1. **Right**: sampled C^0 and C^1 diagnostics from Corollary 2.1 on $K = [0.25L_x, 0.75L_x] \times [0.25L_y, 0.75L_y]$. Solid curves connect the certified numerical values; dashed lines are slope-one guides anchored to the data.

so that there are three interior cathode-anode jump points. The nonrectangular tests use the corrugated-top domain

$$\Omega_{\mathrm{cor}} = \{(x, y) : 0 < x < L_x,\ 0 < y < H(x)\},$$
$$H(x) = L_y \left(1 + 0.22 \sin \frac{2\pi x}{L_x} + 0.10 \sin\left(\frac{4\pi x}{L_x} + 0.5\right)\right),$$

with reactions imposed on the bottom side and homogeneous Neumann data on the remaining boundary. The corrugated $N = 4$ and $N = 6$ tests use alternating Γ_c and Γ_a intervals on the bottom side, with jump locations

$$0.18L_x,\ 0.39L_x,\ 0.60L_x,\ 0.81L_x$$

and

$$0.12L_x,\ 0.27L_x,\ 0.40L_x,\ 0.55L_x,\ 0.70L_x,\ 0.84L_x,$$

respectively. The corrugated domains are included as nonrectangular curvilinear-polygonal tests within the geometric setting of the theory; the cathode-anode junctions themselves remain smooth flat-boundary points, separated from the zero-flux boundary, so they preserve the local structure that determines the logarithmic coefficient.

The corrugated experiment with four jump points is closer to the limiting regime, reaching $R_E = 0.938$ at $\kappa = 5 \times 10^{-6}$. Figure 6 gives the corrugated $N = 6$ run; its certified ratio reaches 0.943 at $\kappa = 3 \times 10^{-7}$.

Figure 7 repeats the corrugated tests with parameter ratios from a ZrO_2-coated stainless-steel study [23]. The retained data reach $R_E = 0.978$ for $N = 4$ and $R_E = 0.950$ for $N = 6$ at $\kappa = 5 \times 10^{-7}$; the next point is excluded by the residual certificate. These parameter-variant runs are therefore used only as robustness checks.

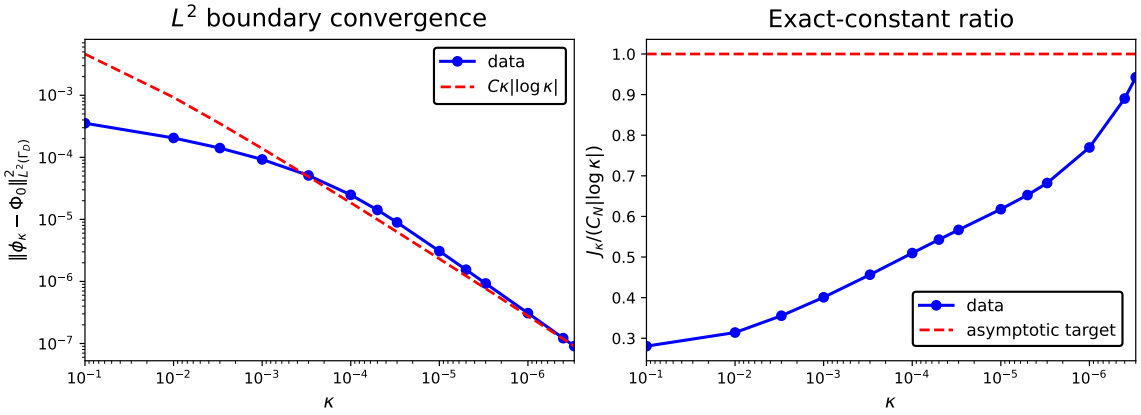

FIGURE 6. Corrugated six-jump diagnostics. **Left**: L^2 boundary convergence to Φ_0 over the admissible data. **Right**: the normalized exact-constant ratio in the theorem-facing window. The retained points show the finite-window approach of $R_E(\kappa)$ toward the predicted unit limit while excluding smaller runs that fail the residual or range certificate.

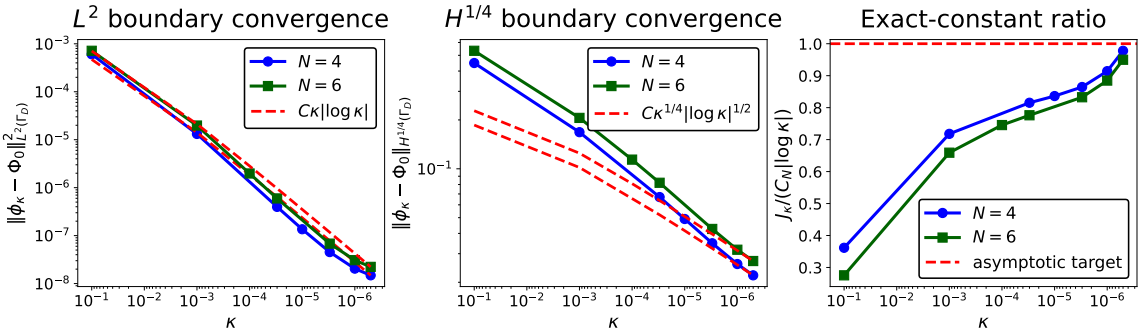

FIGURE 7. Corrugated four- and six-jump diagnostics with one-layer ZrO_2-coated stainless-steel parameter ratios from [23]. The first two panels compare L^2 and $H^{1/4}$ boundary convergence for $N = 4$ and $N = 6$; the right panel shows that the energy ratios remain close to the same exact-constant normalization over the range.

5.4. **Mesh rule.** The mesh rule suggests $h_{\min} \simeq \kappa$ near each smooth jump point. We use the single-jump rectangle for the quantitative mesh-comparison errors and the corrugated four-jump geometry for the mesh visualization.

For each target conductivity we compare three meshes:

- **Uniform (N nodes)**: uniform mesh with the same node count as the graded mesh.
- **Uniform ($4N$ nodes)**: uniform mesh with roughly four times as many nodes.
- **Graded (N nodes)**: local point refinement centered at the boundary jump, with $h_{\min} = 0.25\,\kappa$.

More precisely, if $z_j = (x_j, 0)$ is a boundary jump point, the numerical graded mesh adds the points

$$z_{j,m,\ell} = (x_j + d_m \cos\theta_\ell,\ d_m \sin\theta_\ell), \qquad d_m = h_{\min} m^2, \qquad \theta_\ell = \frac{\ell\pi}{16},$$

for all $m \geq 1$ such that $d_m \leq R_{\text{num}} = 4.0 \times 10^{-3}\,\text{m}$ and for $\ell = 0, \ldots, 16$, retaining only points in the domain. These points are added to a coarse background grid and then triangulated.

Figure 8 shows the same corrugated four-junction geometry on a coarser mesh, so that the grading pattern is visible. Both displayed meshes use $N = 435$ nodes. The left panel uses uniform x- and y-coordinates, while the right panel uses local pointwise refinement around the boundary junction points $z_j = (x_j, 0)$. With $R = 1.6 \times 10^{-3}\,\text{m}$, $M = 7$, $L = 11$, and $q = 2$, set

$$x_j \in \{0.0036,\ 0.0078,\ 0.0120,\ 0.0162\}\,\text{m}, \qquad d_m = R\left(\frac{m}{M}\right)^q, \qquad \theta_\ell = \frac{\ell\pi}{L}.$$

The local refinement points are

$$z_{j,m,\ell} = (x_j + d_m \cos\theta_\ell,\ d_m \sin\theta_\ell), \qquad m = 1, \ldots, M, \quad \ell = 0, \ldots, L,$$

retaining only points in $(0, L_x) \times [0, L_y]$. They are added to a coarse background grid and triangulated in the reference rectangle. For the corrugated domain, the resulting reference mesh is mapped by

$$(x, y) \longmapsto \left(x, \frac{y}{L_y} H(x)\right),$$

with H as in Subsection 5.3. This places the smallest elements near the points $(x_j, 0)$, not along the full vertical lines $x = x_j$.

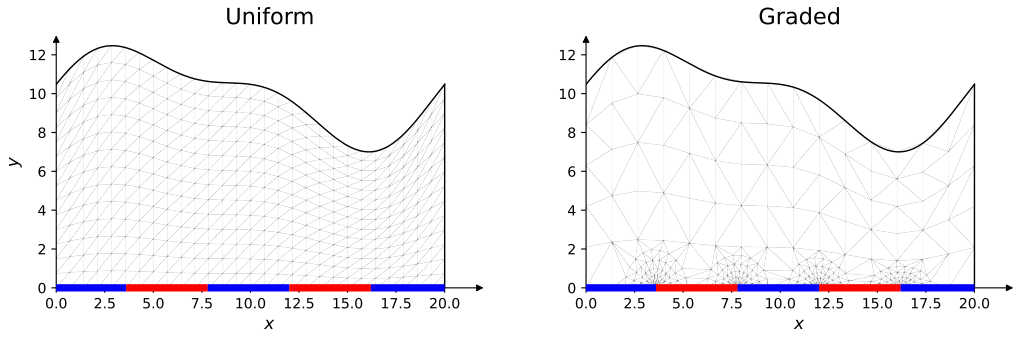

FIGURE 8. Coarsened mesh visualization for the corrugated four-junction geometry. The blue and red boundary segments mark the two prescribed values of Φ_0; the graded mesh concentrates elements near the cathode-anode junctions.

In the single-jump rectangle, errors are measured against a reference solution ϕ_{κ,h_*} computed on the same problem with $h_{\min} = 0.05\,\kappa$ at the boundary jump.

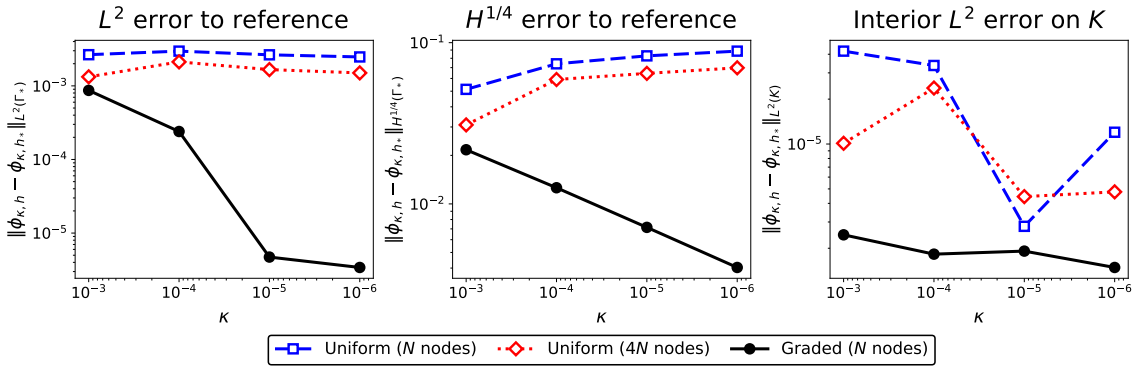

FIGURE 9. Single-jump mesh comparison. **Left**: boundary L^2 error $\|\phi_{\kappa,h} - \phi_{\kappa,h_*}\|_{L^2(\Gamma_*)}$ against an over-resolved graded reference. **Middle**: boundary $H^{1/4}$ error against the same reference. **Right**: interior L^2 error on the inset rectangle K. The graded mesh (black, solid) matches or beats the $4N$-uniform mesh (red, dotted) on all three diagnostics while using the same node budget as the N-uniform mesh (blue, dashed).

Figure 9 shows the payoff of grading. At $\kappa = 10^{-5}$ the graded mesh uses 930 nodes and reaches boundary error 4.7×10^{-6}, while the $4N$ uniform mesh uses 3,655 nodes and remains near 1.7×10^{-3}. The energy ratio behaves similarly: it stays in the predicted band 0.59–0.77 on graded meshes but already rises to about 18 and 9 on the two uniform meshes at $\kappa = 10^{-5}$.

6. Conclusions and future directions

This work shows that the low-conductivity singular limit is controlled by a boundary layer localized at points where Γ_a and Γ_c meet. The stiff boundary reaction drives the trace on $\Gamma_a \cup \Gamma_c$ toward the piecewise equilibrium state, and the interior potential is then selected by the mixed harmonic field associated with that limiting boundary datum. The central point is that the leading energy growth is not a global feature of the whole domain geometry, but a local logarithmic contribution from each smooth boundary jump.

The supporting analysis separates what is standard from what is singular. Solvability and regularity follow from trace-critical variational estimates and classical elliptic theory, while the singular behavior comes from the borderline cost of smoothing a boundary jump.

The numerical experiments are designed around this distinction. They display the formation of the trace layer, compare the nonlinear solutions with the harmonic limit, test the boundary and interior convergence diagnostics, and show the same mechanism in a corrugated geometry with several boundary jumps.

We close by highlighting several directions in which the present analysis can be extended, and which we plan to investigate in future work.

- **Variable conductivity.** Spatially varying conductivity would couple the local jump energy to an inhomogeneous interior metric and could change both the local cell problem and the harmonic selection principle. The most

interesting regime is one in which the conductivity varies on comparable scales to the reaction layer, since then homogenization and jump asymptotics would no longer decouple cleanly.

- **Singular perturbations of the domain and moving boundaries.** Since the leading constant is local at the cathode-anode junctions, it should be stable under smooth perturbations of the domain and of the reaction partition. A quantitative version of this stability would be useful for corrosion models in which the boundary evolves and the elliptic problem is solved on a slowly varying sequence of domains [28, 13].
- **Mixed and nonsmooth geometries.** It would be useful to remove or weaken the separation assumption in the mixed problem, where points of $\overline{\Gamma_a} \cap \overline{\Gamma_c}$ are kept away from changes of boundary type. A related extension is to allow the cathode-anode junction itself to lie at a corner. In a wedge of opening angle α, the local angular profile suggests the leading contribution

$$\frac{(\phi_c - \phi_a)^2}{2\alpha} |\log \kappa|$$

per corner junction, replacing the smooth-boundary denominator 2π. Thus nonsmooth junctions should be governed by the same boundary-layer mechanism, but with the local angle entering the exact constant.

Acknowledgments

The author acknowledges funding from Schaeffler AG & Co. KG. The author thanks Enrique Zuazua for insightful discussions.

References

[1] R.A. Adams and J.J.F. Fournier. *Sobolev Spaces*, volume 140 of *Pure and Applied Mathematics*. Academic Press, Amsterdam, 2nd edition, 2003.

[2] C. Bandle, M.A. Pozio, and A. Tesei. Existence and uniqueness of solutions of nonlinear Neumann problems. *Mathematische Zeitschrift*, 199(2):257–278, 1988.

[3] A.J. Bard and L.R. Faulkner. *Electrochemical Methods: Fundamentals and Applications*. Wiley, New York, 2nd edition, 2001.

[4] Y.S. Bhat and S. Moskow. Homogenization of a nonlinear elliptic boundary value problem modeling galvanic currents. *Multiscale Modeling & Simulation*, 5(1):149–169, 2006.

[5] R. Brown. The mixed problem for Laplace's equation in a class of Lipschitz domains. *Communications in Partial Differential Equations*, 19(7-8):1217–1233, 1994.

[6] A. Cianchi. Moser-Trudinger trace inequalities. *Advances in Mathematics*, 217(5):2005–2044, 2008.

[7] J. Dávila, M. del Pino, M. Musso, and J. Wei. Singular limits of a two-dimensional boundary value problem arising in corrosion modelling. *Archive for Rational Mechanics and Analysis*, 182(2):181–221, 2006.

[8] E. Di Nezza, G. Palatucci, and E. Valdinoci. Hitchhiker's guide to the fractional Sobolev spaces. *Bulletin des Sciences Mathématiques*, 136(5):521–573, 2012.

[9] H. Gao, L. Ju, X. Li, and R. Duddu. A space-time adaptive finite element method with exponential time integrator for the phase field model of pitting corrosion. *Journal of Computational Physics*, 406:109191, 2020.

[10] D. Gilbarg and N.S. Trudinger. *Elliptic Partial Differential Equations of Second Order*. Classics in Mathematics. Springer, Berlin, 2nd edition, 2001.

[11] P. Grisvard. *Elliptic Problems in Nonsmooth Domains*, volume 69 of *Classics in Applied Mathematics*. SIAM, Philadelphia, 2011.
[12] Y.-X. Guo and J.-Q. Liu. Blow-up analysis for solutions of the Laplacian equation with exponential Neumann boundary condition in dimension two. *Communications in Contemporary Mathematics*, 8(6):737–761, 2006.
[13] O. Kavian and M. Vogelius. On the existence and 'blow-up' of solutions to a two-dimensional nonlinear boundary-value problem arising in corrosion modelling. *Proceedings of the Royal Society of Edinburgh: Section A Mathematics*, 133(1):119–149, 2003.
[14] C.E. Kenig. *Harmonic Analysis Techniques for Second Order Elliptic Boundary Value Problems*, volume 83 of *CBMS Regional Conference Series in Mathematics*. AMS, Providence, RI, 1994.
[15] Y. Li and P. Liu. A Moser-Trudinger inequality on the boundary of a compact Riemann surface. *Mathematische Zeitschrift*, 250(2):363–386, 2005.
[16] J.-L. Lions and E. Magenes. *Non-Homogeneous Boundary Value Problems and Applications, Vol. I*, volume 181 of *Die Grundlehren der Mathematischen Wissenschaften*. Springer, Berlin, 1972.
[17] C. Liu and R.G. Kelly. A review of the application of finite element method (fem) to localized corrosion modeling. *Corrosion*, 75(11):1285–1299, 2019.
[18] E. Martínez-Pañeda. Phase-field simulations opening new horizons in corrosion research. *MRS Bulletin*, 49(6):603–612, 2024.
[19] V. Maz'ya. *Sobolev Spaces with Applications to Elliptic Partial Differential Equations*, volume 342 of *Grundlehren der Mathematischen Wissenschaften*. Springer, Berlin, 2nd edition, 2011.
[20] J. Newman and K.E. Thomas-Alyea. *Electrochemical Systems*. Wiley-Interscience, Hoboken, NJ, 3rd edition, 2004.
[21] K.A. Ott and R.M. Brown. The mixed problem for the Laplacian in Lipschitz domains. *Potential Analysis*, 38(4):1333–1364, 2013.
[22] C.D. Pagani, D. Pierotti, A. Pistoia, and G. Vaira. Concentration along geodesics for a nonlinear Steklov problem arising in corrosion modeling. *SIAM Journal on Mathematical Analysis*, 48(2):1085–1108, 2016.
[23] Jingsi Peng, Guojun Ji, Zhiming Shi, and Xiaohuan Wang. Numerical simulation based on a ZrO_2-coated stainless-steel corrosion experiment. *ACS Omega*, 6(22):14504–14517, 2021.
[24] I. Rubinstein. *Electro-Diffusion of Ions*. SIAM, Philadelphia, 1990.
[25] E. Sandier and S. Serfaty. *Vortices in the Magnetic Ginzburg–Landau Model*, volume 70 of *Progress in Nonlinear Differential Equations and Their Applications*. Birkhäuser, Boston, 2007.
[26] S. Scheiner and C. Hellmich. Finite volume model for diffusion- and activation-controlled pitting corrosion of stainless steel. *Computer Methods in Applied Mechanics and Engineering*, 198(37-40):2898–2910, 2009.
[27] J.L. Taylor, K.A. Ott, and R.M. Brown. The mixed problem in Lipschitz domains with general decompositions of the boundary. *Transactions of the American Mathematical Society*, 365(6):2895–2930, 2013.
[28] M. Vogelius and J.-M. Xu. A nonlinear elliptic boundary value problem related to corrosion modeling. *Quarterly of Applied Mathematics*, 56(3):479–505, 1998.
[29] Y. Yang. Moser-Trudinger trace inequalities on a compact Riemannian surface with boundary. *Pacific Journal of Mathematics*, 227(1):177–200, 2006.
[30] Y. Yang. A sharp form of trace Moser-Trudinger inequality on compact Riemannian surface with boundary. *Mathematische Zeitschrift*, 255(2):373–392, 2007.
[31] J. Zhao, S. Jafarzadeh, M. Rahmani, Z. Chen, Y.R. Kim, and F. Bobaru. A peridynamic model for galvanic corrosion and fracture. *Electrochimica Acta*, 391:138968, 2021.

Appendix A. Modeling reduction and nondimensional conductivity

This appendix records the reduced electrochemical scaling behind (1.1). It is not used in the proofs, but it fixes the physical meaning of the small parameter.

The stationary reduction assumes constant conductivity, electroneutral transport, negligible concentration polarization, and a fixed boundary partition, as in activation-controlled potential models for galvanic corrosion [20, 24].

Let Φ_{phys} be the dimensional electrolyte potential. In a well-mixed electrolyte with electroneutrality in the electrolyte interior and negligible concentration polarization, Ohm's law gives the current density

$$j = -\sigma \nabla \Phi_{\mathrm{phys}},$$

where $\sigma > 0$ is the electrolyte conductivity. Charge conservation gives

$$\operatorname{div} j = 0, \qquad \text{hence} \qquad -\Delta \Phi_{\mathrm{phys}} = 0$$

when σ is constant. On an insulating boundary component, $j \cdot \nu = 0$. On a reactive metal-electrolyte interface, the normal current is modeled by a signed exponential current-overpotential law

$$j \cdot \nu = i_{*,0} \left[\exp\left(\frac{(1-\alpha) z F (\Phi_{\mathrm{phys}} - E_*)}{RT} \right) - \exp\left(-\frac{\alpha z F (\Phi_{\mathrm{phys}} - E_*)}{RT} \right) \right],$$

with the equilibrium potential E_* and exchange current $i_{*,0}$ chosen according to the reactive process. Here $\alpha \in (0,1)$ is the transfer coefficient, z is the charge number, F is Faraday's constant, R is the gas constant, and T is the absolute temperature.

Choose a length scale L and a potential scale V. Write

$$x = L\widehat{x}, \qquad \Phi_{\mathrm{phys}} = V\phi.$$

Then the boundary condition becomes

$$\partial_{\widehat{\nu}} \phi = -\frac{L i_{*,0}}{\sigma V} \widehat{i}_*(\phi),$$

up to the sign convention for the outward normal and with $\widehat{i}_*$ denoting the corresponding dimensionless signed exponential current. After absorbing fixed exchange-current ratios and thermal-voltage constants into the dimensionless currents i_a and i_c, the common conductivity parameter used in the paper is

$$\kappa := \frac{\sigma V}{L i_{\mathrm{ref}}},$$

where i_{ref} is the reference exchange-current scale. Thus the low-conductivity regime $\kappa \to 0^+$ corresponds either to decreasing electrolyte conductivity, increasing device length, or increasing interfacial exchange-current scale relative to Ohmic transport through the electrolyte interior. In this regime the dimensionless model takes the form

$$\partial_\nu \phi = -\frac{i_a(\phi)}{\kappa} \quad \text{on } \Gamma_a, \qquad \partial_\nu \phi = -\frac{i_c(\phi)}{\kappa} \quad \text{on } \Gamma_c,$$

which is (1.1). The mathematical analysis in the paper treats this reduced stationary problem; concentration dynamics, space-charge layers, and moving-interface effects are outside the model and are listed as extensions in Section 6.